# Transient Measurements and Simulations Correlate Exchange Ligand Concentration and Trap States in Colloidal Quantum Dot Photodetectors

Darshan H. Parmar,[‡] Benjamin Rehl,[‡] Ozan Atan,[‡] Sjoerd Hoogland, and Edward H. Sargent*

Cite This: https://doi.org/10.1021/acsami.3c14611

Read Online

ACCESS | 📊 Metrics & More | 📑 Article Recommendations | 🆔 Supporting Information

**ABSTRACT:** Colloidal quantum dot (CQD) photodetectors (PDs) can detect wavelengths longer than the 1100 nm limit of silicon because of their highly tunable bandgaps. CQD PDs are acutely affected by the ligands that separate adjacent dots in a CQD-solid. Optimizing the exchange solution ligand concentration in the processing steps is crucial to achieving high photodetector performance. However, the complex mix of chemistry and optoelectronics involved in CQD PDs means that the effects of the exchange solution ligand concentration on device physics are poorly understood. Here we report direct correspondence between simulated and experimental transient photocurrent responses in CQD PDs. For both deficient and excess conditions, our model demonstrated the experimental changes to the transient photo-



current aligned with changes in trap state density. Combining transient photoluminescence, absorption, and photocurrent with this simulation model, we revealed that different mechanisms are responsible for the increased trap density induced by excess and deficient active layer ligand concentrations.

**KEYWORDS:** *lead sulfide quantum dots, mixed halide passivation, quantum dot photodetector, ligand concentration, trap state density, transient, steady state, Setfos simulation*
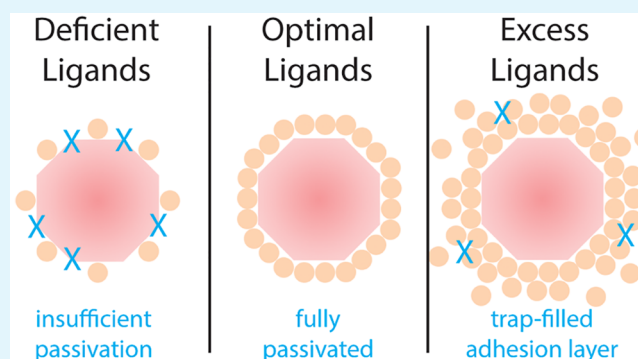
## INTRODUCTION

Wavelengths longer than 1100 nm are crucial to depth sensing, optical communications, and bioimaging applications as they use optical bands that fall within the "water-window" where absorption from ambient water is minimal.[1,2] Colloidal quantum dot (CQD) photodetectors can detect short-wave infrared (SWIR) light beyond the silicon absorption limit, making them attractive candidates for these applications. CQDs are a versatile class of semiconductors with tunable bandgaps and thus tunable absorption wavelengths.[3,4] In addition, CQDs are solution-processed, which reduces cost compared to the single crystal epitaxial growth of conventional IR-sensitizers (i.e., InGaAs, Ge) and does not hinder integration with silicon readout circuits. However, the CQD surface properties play a key role in the performance of CQD-based photodetectors. In particular, the CQD ligands modulate these surface properties, such as trap state density.

During synthesis, long-chain organic capping ligands prevent CQD aggregation and allow dots to grow into well-separated nanocrystals. To fabricate optoelectronic devices, these long-chain, insulating ligands are exchanged with shorter, more conductive ligands to improve charge carrier mobility in the CQD films.[3,4] While there have been works discussing the effects of these smaller ligands' reactivity and chemistry, there

have been few reports on the effect of ligand concentration during the solution exchange process on the final device performance.[5−7] Ligand concentrations for ligand exchange solutions is typically optimized in CQD studies; therefore, we seek to study this process in more detail.[8]

It is generally assumed that a small number of ligands form a monatomic adlayer with the quantum dot surface, while excess ligands are removed during the washing steps and therefore do not interfere with the CQD solid. Yet, a highly concentrated exchange solution with excess ligands does not yield the best performance. Instead, carefully optimizing the ligand concentration has been vital to achieving high performance CQD devices.[8] The mechanism behind the need for this optimization is not fully understood, in particular, when using an excess ligand concentration. Here we combine simulation and experimental measurements in both transient

and steady-state regimes to investigate the effect of ligand concentration during ligand exchange on the CQD photodetector performance. Our combined experimental and simulation study reinforces our understanding of the nonmonotonic relationship between ligand concentration during ligand exchange and trap state density that directly affects dark current, external quantum efficiency (EQE), and transient photocurrent fall times. We show that a deficiency and an excess of ligands in the exchange step lead to different mechanisms for increasing the active layer trap density.

### RESULTS AND DISCUSSION

**Charge Carrier Dynamics Suggest Increasing Trap Density with Suboptimal Ligand Concentration Conditions.** A two-phase liquid ligand exchange was performed to replace the native oleic acid ligands of PbS CQD with an excitonic peak around 1350 nm with a mixture of halide ligands. An exchange solution using a 5:4:5:4.4 molar ratio of $PbCl_2$, $PbBr_2$, $PbI_2$, and sodium acetate was identified in prior studies to maximize surface coverage.[9] Chloride and bromide ions have been associated with the passivation of the Pb (100) facet, which affects the CQD trap density.[5,10] The relatively larger iodide ions have been associated with the passivation of the Pb (111) surface, which has been attributed to improved charge transport and charge carrier mobility in CQD films.[5,11] Here, we varied the concentration by changing only the $PbCl_2$ and $PbBr_2$ concentrations (see Table S1 for details) to study the relationship between the PbS CQD trap density without significantly affecting the charge transport associated with the Pb (111) surface. We investigated CQD inks and films made from three different total ligand concentrations to represent three regimes of CQD passivation: deficient, optimal, and excess. Respectively, we used concentrations of 120, 140, and 180 mM by reducing the concentration of $PbCl_2$ and $PbBr_2$ from our previously reported values.[5]

The absorbance and photoluminescence (PL) of CQD films spin coated on glass/ITO substrates prepared by using different ligand concentrations were measured to gain insight into the effect on trap density (Figure 1A,B). A higher density of trap states increases the probability of nonradiative decay of charge carriers to lower energy levels within the bandgap which produces a red shift in the emission wavelength relative to the band edge. Although energy transfer due to CQD crowding is also known to increase the Stokes shift with optical density,[12] for samples of similar optical density a relatively larger red shift therefore suggests a higher trap density or deeper traps are present in the material.[13,14] We observed differences in the Stokes shifts for the three ligand concentrations: films derived from the 140 mM ligand exchange solution had the smallest Stokes shift of 61 nm; films made from 180 mM had a larger shift of 65 nm; and films made from 120 mM had the largest Stokes shift of 85 nm. Additionally, we observed a small peak on the low energy side of the photoluminescence spectrum. We attribute this peak to trap-assisted radiative recombination due to traps within the bandgap. We note that this peak is the largest for the CQD prepared under deficient ligand concentrations.

Transient PL was measured to gain further insight into the trap density (Figure 1B). An increase in PL lifetime suggests a decrease in trap density (and vice versa) as lower trap density means less recombination centers for the charge carriers.[15−17] We observed the same nonmonotonic trend in the PL decay as with the Stokes shifts: The 120 and 140 mM ligand exchange
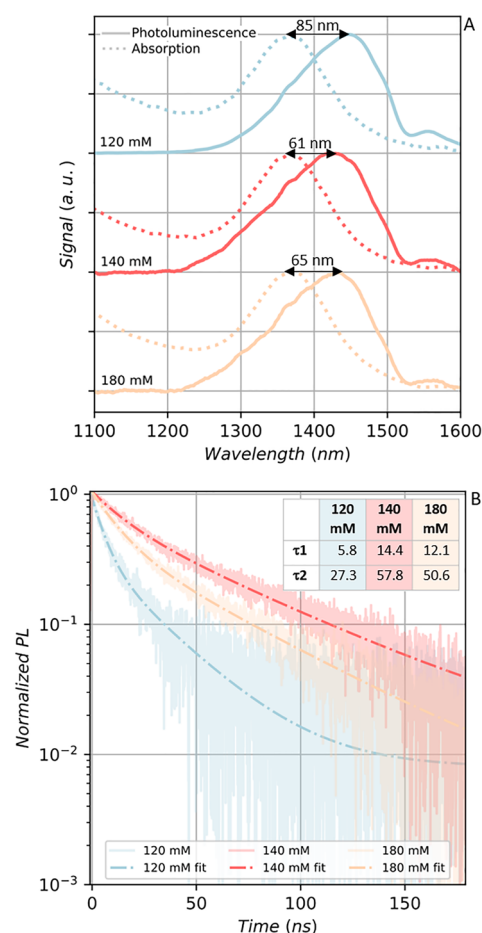


**Figure 1.** A) Normalized optical absorption (dotted line) and photoluminescence (solid line) of 120, 140, and 180 mM ligand concentration quantum dot colloids, respectively. B) TRPL measurements showing PL decay over time for the three ligand concentrations and corresponding fitting (dashed line). PL lifetimes extracted from the fits are tabulated.

solutions had the fastest and slowest decays, respectively. In all cases, the transient PL fit well to a biexponential consisting of a slower and faster component, which we attribute to radiative and nonradiative recombination, respectively. In addition to the lifetimes of both short and fast components, the ratio of slow to fast component amplitude also followed the nonmonotonic trend ($A_{slow}/A_{fast}$ = 0.61, 1.7, and 0.78 for 120, 140, and 180 mM, respectively). Therefore, the relative amount of nonradiative recombination was the largest for the 120 mM sample and the smallest for the 140 mM sample. Yet, despite this similar ratio of nonradiative to radiative recombination amplitudes, the PL lifetimes of the 180 mM sample were twice as long as the 120 mM case and similar to the 140 mM case. This difference in PL lifetimes and similarity in amplitude ratios between 180 and 120 mM suggests different trap state origins. Overall, these findings support the hypothesis of an optimal ligand concentration (between 120 and 180 mM), which yielded the longest-lived PL.

To further investigate the nonradiative relaxation pathways with respect to ligand concentration, transient absorption measurements were conducted with increasing pump power. For each ligand concentration, a single bleach was observed around 1330 nm (Figure 2A−C), which lies within the steady state absorbance peak. With increasing pump power, the
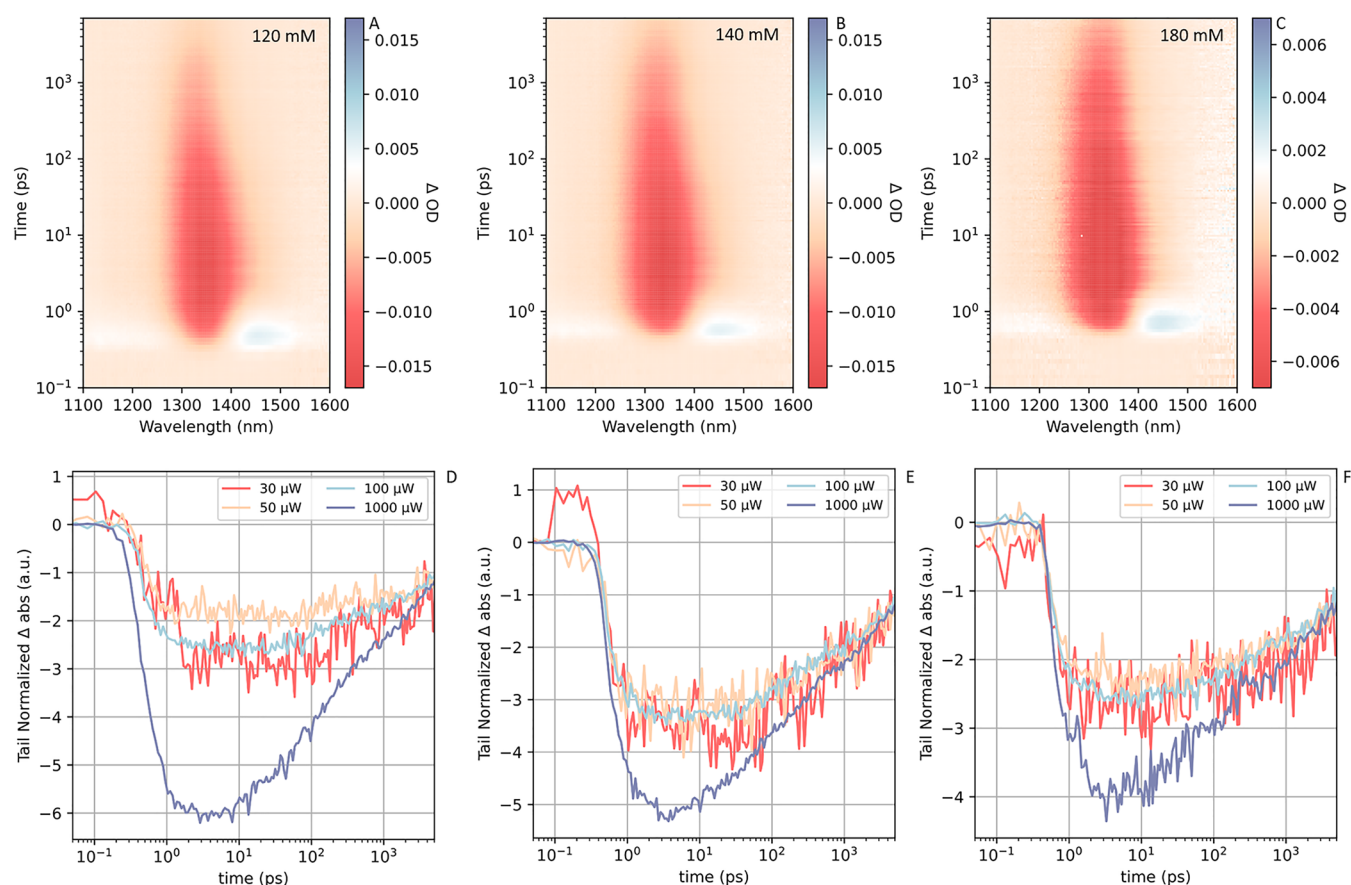
**Figure 2.** 2D plots of the transient absorption spectra (1100−1600 nm) from 100 fs −7.5 ns for CQD prepared from A) 120 mM, B) 140 mM, and C) 180 mM ligand concentration. Tail-normalized 1330 nm bleach dynamics with increasing pump power from 30−1000 $\mu$W for CQD prepared from D) 120 mM, E) 140 mM, and F) 180 mM ligand concentration.

bleach amplitude increased but the bleach dynamics remained relatively consistent until 1000 $\mu$W. The tail-normalized transient bleach (Figure 2D−F) demonstrates these consistent dynamics from 30 to 100 uW of pump power assuming one exciton per dot at relatively long delay time. However, at 1000 $\mu$W pump power, a new component to the bleach appeared for all ligand concentrations. We tentatively attribute this new component to multiexciton generation and Auger recombination owing to its appearance at high pump power and short lifetime. Since Auger recombination is a multibody phenomenon, it is more pronounced at higher charge carrier concentrations and higher density of states.[18−20] The magnitude of this fast component was the greatest for 120 mM and similar for 140 and 180 mM. We attribute more Auger recombination with a lower ligand concentration to insufficient ligand coverage and therefore partial trap passivation. Furthermore, partial CQD passivation in films results in adjacent dots being in closer proximity and may result in dot fusion or aggregation.[5] This poorer passivation and increased proximity increase the density of states at the band edge, leading to more Auger recombination. Similar Auger contributions at 140 and 180 mM suggest a similar density of states at the band edge indicating that CQDs at both concentrations are sufficiently passivated and separated by at least a monolayer of ligands.

**Photodetector Performance and Simulation.** To explore the device-level effects of ligand concentration, we fabricated a PIN structure to build upon prior studies for improving transient photocurrent fall times.[9] Specifically, we improved on a prior device structure that used NiOx as the HTL by introducing a 25 nm layer of PbS CQDs with an excitonic peak at 950 nm capped with ethane-1,2-dithiol (EDT) in the hole transport structure (HTS). For the electron transport layer (ETL), trans-4-(trifluoromethyl) cinnamic acid (TFCA) capped PbS CQDs with an excitonic peak of 950 nm were used as TFCA has been shown to provide n-type doping in PbS CQDs while also improving passivation and operational stability.[21] The conduction band minima (CBM), valence band maxima (VBM), were collected from the literature (see Table S3) and noted in Figure 3A. The HTS and ETL create a potential gradient across the active layer, which is responsible for the built-in electric field needed for photodetectors. The high CBM of NiOx results in electron blocking, and conversely, the low VBM of the TFCA-capped CQDs results in hole blocking. Finally, indium tin oxide (ITO) was used as the transparent electrode and silver was used as the top electrode.

The reverse dark current was the lowest for devices made with 140 mM ligand concentrations (Figure 3C). Increasing the ligand concentration did not reduce the dark current (or saturate it at a minimum) as would be the case if passivation was improved and excess ligands were fully washed away in the supernatant during ink preparation. Decreasing the ligand concentration increased the dark current. While high dark current can be attributed to many phenomena, it is widely observed that high trap state density is the primary cause of an
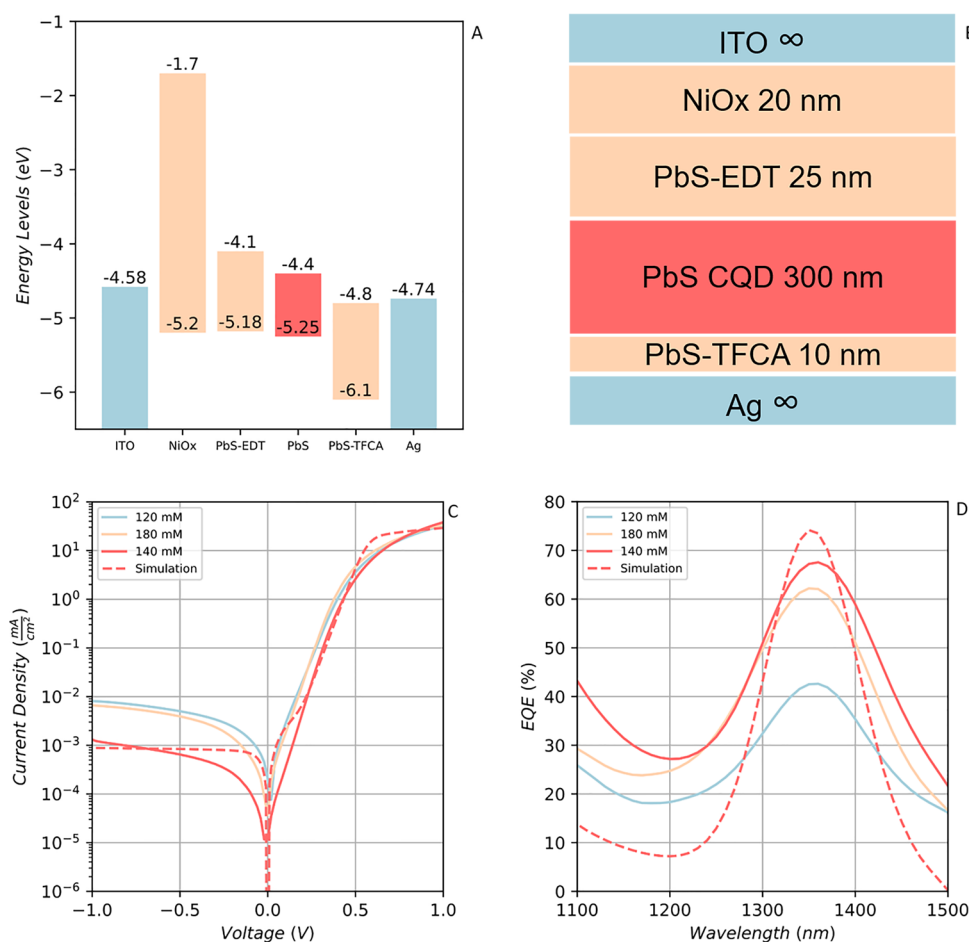
**Figure 3.** A) Band alignment of materials used in photodetector devices. B) Layer thicknesses and device structure. EDT and TFCA were the ligands used in PbS CQDs for the respective layers. C, D) Current−voltage and EQE measurements of photodetector devices made from inks synthesized using 120, 140, and 180 mM ligand concentrations, respectively. Simulated values are shown as dotted line.

increased dark current in solution-processed semiconductor photodetectors.[22−25] Therefore, the increase in dark current with either excess of deficient ligand concentrations reflects an increase in trap density.

Additionally, EQE is another photodetector performance parameter directly affected by trap state density.[26−28] A highest EQE of 68.5% was achieved with the 140 mM ligand exchange (Figure 3D). Decreasing the ligand concentration decreased the EQE. Increasing the ligand concentration did not increase or saturate the EQE at 68.5%. Instead, there was also decrease in the EQE at 180 mM, indicating an optimal ligand concentration between 120 and 180 mM.

To compare our experimental findings, we used commercial software (Setfos, version 5.3, Fluxim AG, Switzerland) for electrical and optical simulations. The model was optimized to match the experimental data for the optimal (140 mM) case. First, a steady-state model was developed to study the device's response under varying bias and illumination conditions (for simulation parameters see Table S3). Then, using the same material parameters, the transient response of the model was studied. After confirming a good match between experimental and simulated IV and EQE in the optimal (140 mM) case (Figure 3C,D dashed lines), we used the model to investigate changes in the active layer properties, in particular, bulk trap density.

**Transient Photocurrent Modulated by Trap Density.** A prevalence of trap states in films prepared under nonoptimal ligand concentrations links our optical and steady state electrical measurements. To further investigate this connection, we studied the transient photocurrent behavior at all three ligand concentrations. Driving an 1100 nm laser with a square wave, we measured the transient response of the photodetector at different illumination intensities (see the experimental section for details). The illumination intensity was increased by increasing the offset voltage driving the laser diode from 600 to 1100 mV.

We observed a biexponential decay in the transient signal (Figure 4A−C). Initially, there was a rapid decay within the first 2 μs to 10% of the original signal, followed by a slow decay to 1% of the signal and beyond. While this fall time pattern was consistent for all illumination powers and ligand concentrations, there were two clear differences between the optimal (140 mM) and suboptimal ligand concentrations (120 and 180 mM).

First, for deficient and excess ligand concentrations, the fall time to 1% photocurrent was more sensitive to illumination intensity than for the optimal concentration. For 120 and 180 mM there was a 10.8 and 5.7 μs difference, respectively, between the fall times of the lowest and highest illumination intensities (Figure 4D). For 140 mM, however, the fall times were less dependent on illumination intensity, as the difference
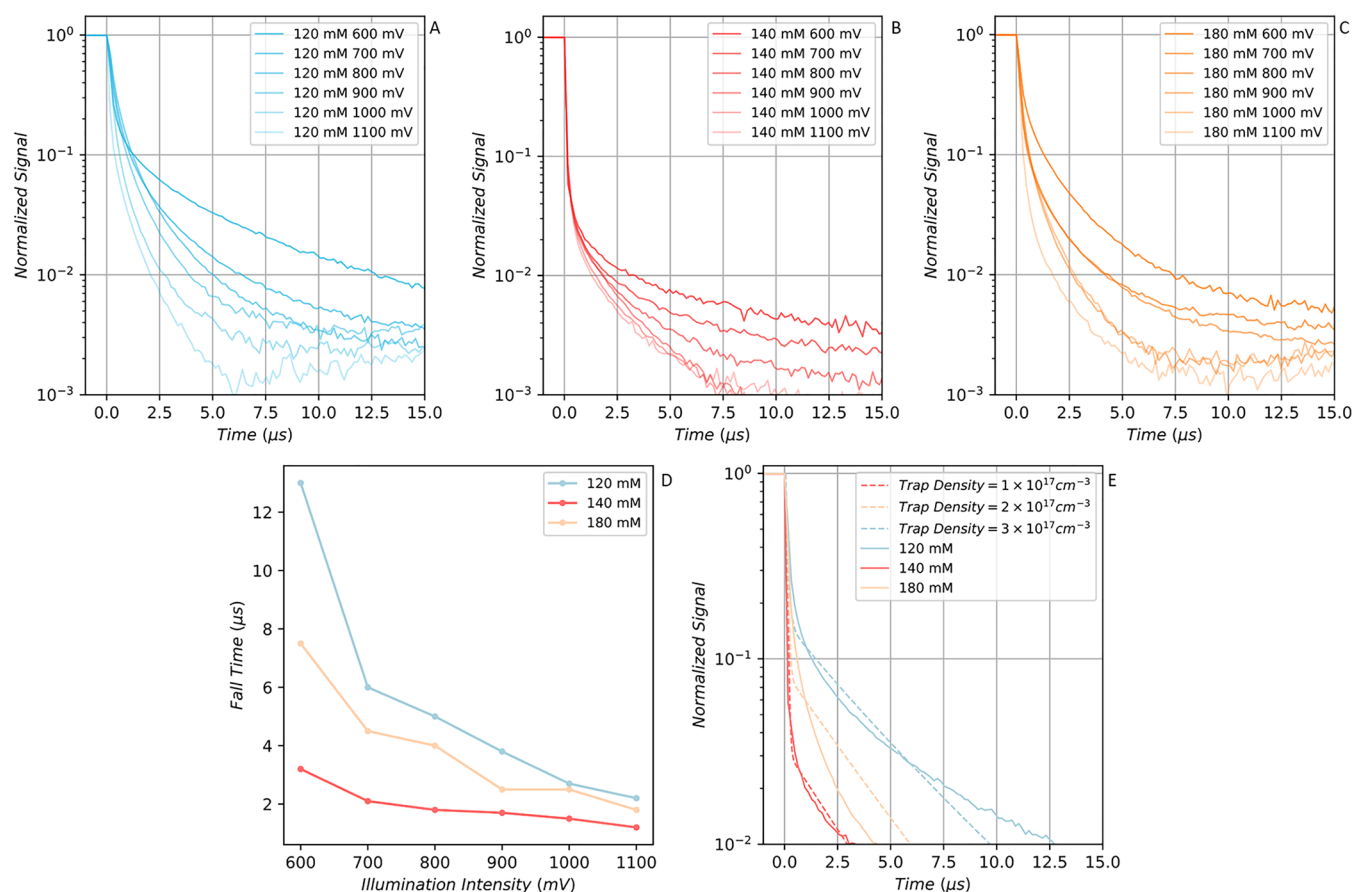
**Figure 4.** A−C) Normalized transient photodetector signal at increasing illumination intensities for devices made from 120, 140, and 180 mM ligand concentrations, respectively. D) Fall time to 1% of normalized signal for each ligand concentration as a function of illumination intensity. E) Normalized transient photodetector signal at 600 mM illumination for the three ligand concentrations. Simulated transient photocurrent traces at various trap densities are shown with dotted lines.

from high to low power was only 1.9 $\mu$s. Furthermore, while the fall times for all ligand concentrations were similar at a higher illumination intensity (1100 mV), they differed drastically at a lower illumination intensity (600 mV). Strong fall time to illumination intensity dependence is indicative of higher trap densities.[22,29,30] At lower illumination intensity, trap states capture photocarriers, slowing their progression to the collecting electrodes and increasing signal fall times. At higher illumination intensities, these trap states are saturated with carriers; thus, there is less hindrance to carrier transport producing faster fall times. When there are fewer traps, this effect is less pronounced. Therefore, the strong dependence of fall times on illumination intensity for 120 and 180 mM compared to 140 mM suggests that the former have a comparatively higher trap density.

Second, the amplitude of the slow component was larger for 140 mM than for 120 or 180 mM (Figure 4E). Overall, a faster signal decay suggests that carriers are less impeded by traps in the 140 mM case than in 120 mM or 180 mM.[9,22,31] To verify our understanding and observations of the link between the ligand concentration and trap states, we conducted Setfos simulations with varying degrees of trap state densities. We found that the simulated transient signals also consisted of a biexponential decay. As with the experimental results, the amplitude of the second component increased with increasing trap density. Tuning the trap densities, we were able to simulate the transient photocurrent of the three ligand

concentrations with a trap density of $1 \times 10^{17}$ cm$^{-3}$ corresponding to 140 mM and higher trap densities of $2 \times 10^{17}$ and $3 \times 10^{17}$ cm$^{-3}$ corresponding to 180 and 120 mM respectively. These trap density values agree with previous reported values of $1.8–2.2 \times 10^{17}$ cm$^{-3}$.[21] This is the first report of agreement between transient simulation and experimental data of CQD photodetectors, demonstrating the utility of simulation in CQD device design.

**Interpretation of Our Findings.** At low ligand concentrations, we observed a higher trap density and Auger recombination. This result suggests incomplete passivation of the quantum dots due to deficient ligand concentration leading to dangling bonds at the surface which can trap charge carriers (Figure S4).[5,28,32] Additionally, the incomplete passivation may reduce the interparticle distance of adjacent dots which further promotes Auger recombination.[5,18−20] Complete passivation due to an optimal ligand concentration leads to a monolayer of ligands surrounding the individual dots. In this case, the ligands form a slight barrier that separates adjacent dots.[5] In this case, there are fewer trap states, and sufficient separation between dots reduces Auger effects. We observed excess ligand concentration leading to similar decreases to PL lifetime and increases to photocurrent fall time as deficient ligand concentration. However, adjacent dots should be well-separated in the excess ligand case, which hinders Auger effects and was reflected in the transient absorption measurements. The presence of high trap densities despite sufficient

CQD coverage suggests that the traps appear in a barrier region formed by the ligands. Further studies are required to verify this interpretation of traps in the barrier region; however, tentatively we suggest that excess ligand concentration leads to a trap-filled adhesion layer of ligands around the quantum dot. The presence of this layer is supported by XPS measurements of the CQD films, which showed an increase in bromide and chloride content with increasing ligand exchange concentrations (Figure S1).

## CONCLUSION

In summary, we used transient photoluminescence, absorption, and photocurrent to understand the origin of poor performance in devices made with CQD ink prepared by using excess and deficient ligand concentrations. Comparing both steady state and transient simulations and experiments, we determined that inks prepared with 15−30% excess or deficient ligand concentration resulted in two to three times increased trap density. Excess and deficient ligand concentrations are both detrimental to photodetector performance, yet our study reveals that the mechanisms are different for the two cases. For deficient ligands, we attribute the increases in trap density to incomplete passivation. For excess ligands, we suggest the presence of a trap-filled adhesion layer. We believe these findings will lead to a more precise tuning of CQD photodetector properties.

## EXPERIMENTAL METHODS

**Synthesis and Exchange of PbS CQD.** PbS CQDs were synthesized using previously published methods.[33] A liquid phase ligand exchange was performed to replace the native oleic acid ligands with hybrid halide ligands. Ligand concentrations of 120, 140, and 180 mM were used. An ink was made from the ligand exchanged CQDs for spin coating. Ligand exchange and ink preparation was done using published methods.[9]

**Device Fabrication.** Glass substrates with predeposited ITO were cleaned in an ultrasonic bath using deionized water for 60 min, using with acetone for 30 min, and finally using isopropyl alcohol for minutes. The substrates were dried before the HTL deposition. NiOx was deposited using a previously developed sputtering process.[9] EDT-caped PbS were deposited on top of the NiOx using a previously reported solid-state ligand exchange.[22] The active layer was spin-coated onto the HTL-deposited substrates by spin-coating 50 $\mu$L of CQD ink at 2000 rpm for 60 s under a flow of nitrogen. The deposited films were annealed at 70 °C in a nitrogen-filled glovebox for 15 min. A previously reported ligand exchange was used to deposit TFCA-capped PbS CQDs on top of the active layer.[21] A 120 nm layer of silver was deposited by using thermal evaporation to form the top electrode. Masks were used to define circular devices of areas 4.9, 1.54, 0.79, 0.20, 0.03, and 0.008 mm$^2$.

**Optical Characterization.** To measure absorption spectra, the light from a stabilized fiber-coupled light source (THORLABS, SLS201L) was passed through the sample and then collected via a fiber in a spectrometer (Ocean Optics Inc., NIR-512).

Photoluminescence spectra and lifetimes were measured using a Fluorolog TCSPC instrument (HORIBA Scientific). The samples were excited using a DD-830L laser diode (DeltaDiode, 100 MHz, 820 nm, HORIBA Scientific) and the reflected photoluminescence was directed toward a grating (iHR320, 600 grooves/mm, 1000 nm blaze wavelength) and monochromator before being detected on a InGaAs photodetector (S1−H10330−75).

To measure transient absorption spectra, femtosecond laser pulses (1030 nm, 5 kHz repetition rate) were produced in a regeneratively amplified Yb:KGW laser (PHAROS, Light Conversion). A portion of the beam was passed through a delay stage (HELIOS, Ultrafast Systems, 8 ns window, 14 fs resolution) and focused into a sapphire

crystal to generate a broad white light continuum probe beam in the NIR, which was directed toward the sample (50 um beam waist). After transiting the sample, the probe light was passed through several filters and focused onto a fiber-coupled spectrometer (Helios, Ultrafast Systems, InGaAs 256 pixels). The remainder of the 1030 nm beam was directed into an optical parametric amplifier (ORPHEUS, Light Conversion) to generate an 820 nm pump beam. This pump beam was passed through an optical chopper wheel to block every second pulse. The pump beam was then focused ($f = 500$ mm) onto the sample and overlapped in space at an angle with respect to the probe light. The power of the pump beam was controlled by using neutral density filter wheels. The samples were continuously translated by using a motorized stage to minimize laser heating effects.

XPS measurements were performed using a Thermo Scientific K-alpha system on ligand exchanged CQD spin coated (1000 rpm, 800 rpm/s$^2$, 10 s, under N$_2$) on precleaned and dried glass slide.

**Electrical Characterization.** Current voltage measurements were made by using a Keithley 2400 source meter. The applied voltage was swept from −1 to 1 V in 0.02 V increments. 4.9 mm$^2$ area devices were used for these measurements. The EQE was measured using the Enlitech Quantum Efficiency Measurement System QE-R under −1 V bias. For transient photocurrent measurements, a 1310 nm laser diode (Thorlabs ML725B8F) was modulated at 10 kHz with a signal generator (Tektronix AFG 31000) to provide illumination. The output signal from the photodetector was passed to a preamplified (Femto DHPCA-100) which was also used to bias the device at −1 V. A 1 GHz oscilloscope (Tektronix 6 series MSO64B) was used to record the output signal. Devices of area 0.79 mm$^2$ were used for these measurements to move to the transport-limited regime rather than the RC-limited regime of large areas. Illumination intensity was altered by changing the offset of the signal generator driving the laser diode.

**Simulation Details.** Setfos, version 5.3, is used for the electrical and optical simulations. Material parameters are chosen based on experimental measurements or available data from the literature about the interested material. Constant electron−hole mobilities are used during the simulations. Trap-assisted recombination is modeled by defining Shockley−Read−-Hall (SRH) centers with appropriate capture rates. Drift-diffusion and absorption modules were used to simulate voltage−current curves, wavelength-dependent EQE and transient response of the device, while parameter sweeping was utilized to study the relationship between the material properties and the results.

## ASSOCIATED CONTENT

**Supporting Information**

The Supporting Information is available free of charge at https://pubs.acs.org/doi/10.1021/acsami.3c14611.

Ligand concentrations, transient photoluminescence fitting parameters, Setfos simulation parameters, XPS data, transient photocurrent comparison of devices with and without NiOx, schematic interpretation of increased trap density mechanisms (PDF)

## AUTHOR INFORMATION

**Corresponding Author**

**Edward H. Sargent** − *The Edward S. Rogers Department of Electrical and Computer Engineering, University of Toronto, Toronto, Ontario M5S 3G4, Canada;* orcid.org/0000-0003-0396-6495; Email: ted.sargent@utoronto.ca

**Authors**

**Darshan H. Parmar** − *The Edward S. Rogers Department of Electrical and Computer Engineering, University of Toronto, Toronto, Ontario M5S 3G4, Canada;* orcid.org/0000-0001-9533-7594

**Benjamin Rehl** − *The Edward S. Rogers Department of Electrical and Computer Engineering, University of Toronto, Toronto, Ontario M5S 3G4, Canada;* ⊙ orcid.org/0000-0002-5534-6717

**Ozan Atan** − *The Edward S. Rogers Department of Electrical and Computer Engineering, University of Toronto, Toronto, Ontario M5S 3G4, Canada;* ⊙ orcid.org/0000-0003-1439-8470

**Sjoerd Hoogland** − *The Edward S. Rogers Department of Electrical and Computer Engineering, University of Toronto, Toronto, Ontario M5S 3G4, Canada;* ⊙ orcid.org/0000-0002-3099-585X

Complete contact information is available at:
https://pubs.acs.org/10.1021/acsami.3c14611

## Author Contributions

‡D.H.P., B.R., and O.A. contributed equally.

## Notes

The authors declare no competing financial interest.

## ■ REFERENCES

(1) Hansen, M. P.; Malchow, D. S. Overview of SWIR Detectors, Cameras, and Applications. *Proc. SPIE* **2008**, *6939*, 94−104.

(2) Breiter, R.; Wendler, J.; Lutz, H.; Rutzinger, S.; Hofmann, K.; Ziegler, J. IR-Detection Modules from SWIR to VLWIR: Performance and Applications. *Proc. SPIE* **2009**, *7298*, 72981W.

(3) Kagan, C. R.; Lifshitz, E.; Sargent, E. H.; Talapin, D. V. Building Devices from Colloidal Quantum Dots. *Science* **2016**, *353* (6302), No. aac5523.

(4) Ip, A. H.; Thon, S. M.; Hoogland, S.; Voznyy, O.; Zhitomirsky, D.; Debnath, R.; Levina, L.; Rollny, L. R.; Carey, G. H.; Fischer, A.; Kemp, K. W.; Kramer, I. J.; Ning, Z.; Labelle, A. J.; Chou, K. W.; Amassian, A.; Sargent, E. H. Hybrid Passivated Colloidal Quantum Dot Solids. *Nat. Nanotechnol.* **2012**, *7* (9), 577−582.

(5) Fan, J. Z.; Andersen, N. T.; Biondi, M.; Todorović, P.; Sun, B.; Ouellette, O.; Abed, J.; Sagar, L. K.; Choi, M.-J.; Hoogland, S.; de Arquer, F. P. G.; Sargent, E. H. Mixed Lead Halide Passivation of Quantum Dots. *Adv. Mater.* **2019**, *31* (48), No. 1904304.

(6) Cao, Y.; Stavrinadis, A.; Lasanta, T.; So, D.; Konstantatos, G. The Role of Surface Passivation for Efficient and Photostable PbS Quantum Dot Solar Cells. *Nat. Energy* **2016**, *1* (4), 1−6.

(7) Malgras, V.; Nattestad, A.; Yamauchi, Y.; Dou, S. X.; Kim, J. H. The Effect of Surface Passivation on the Structure of Sulphur-Rich PbS Colloidal Quantum Dots for Photovoltaic Application. *Nanoscale* **2015**, *7* (13), 5706−5711.

(8) Neo, D. C. J.; Cheng, C.; Stranks, S. D.; Fairclough, S. M.; Kim, J. S.; Kirkland, A. I.; Smith, J. M.; Snaith, H. J.; Assender, H. E.; Watt, A. A. R. Influence of Shell Thickness and Surface Passivation on PbS/CdS Core/Shell Colloidal Quantum Dot Solar Cells. *Chem. Mater.* **2014**, *26* (13), 4004−4013.

(9) Atan, O.; Pina, J. M.; Parmar, D. H.; Xia, P.; Zhang, Y.; Gulsaran, A.; Jung, E. D.; Choi, D.; Imran, M.; Yavuz, M.; Hoogland, S.; Sargent, E. H. Control over Charge Carrier Mobility in the Hole Transport Layer Enables Fast Colloidal Quantum Dot Infrared Photodetectors. *Nano Lett.* **2023**, *23* (10), 4298−4303.

(10) Choi, H.; Ko, J.-H.; Kim, Y.-H.; Jeong, S. Steric-Hindrance-Driven Shape Transition in PbS Quantum Dots: Understanding Size-Dependent Stability. *J. Am. Chem. Soc.* **2013**, *135* (14), 5278−5281.

(11) Lan, X.; Voznyy, O.; García de Arquer, F. P.; Liu, M.; Xu, J.; Proppe, A. H.; Walters, G.; Fan, F.; Tan, H.; Liu, M.; Yang, Z.; Hoogland, S.; Sargent, E. H. 10.6% Certified Colloidal Quantum Dot Solar Cells via Solvent-Polarity-Engineered Halide Passivation. *Nano Lett.* **2016**, *16* (7), 4630−4634.

(12) Voznyy, O.; Levina, L.; Fan, F.; Walters, G.; Fan, J. Z.; Kiani, A.; Ip, A. H.; Thon, S. M.; Proppe, A. H.; Liu, M.; Sargent, E. H. Origins of Stokes Shift in PbS Nanocrystals. *Nano Lett.* **2017**, *17* (12), 7191−7195.

(13) Caram, J. R.; Bertram, S. N.; Utzat, H.; Hess, W. R.; Carr, J. A.; Bischof, T. S.; Beyler, A. P.; Wilson, M. W. B.; Bawendi, M. G. PbS Nanocrystal Emission Is Governed by Multiple Emissive States. *Nano Lett.* **2016**, *16* (10), 6070−6077.

(14) Liu, Y.; Kim, D.; Morris, O. P.; Zhitomirsky, D.; Grossman, J. C. Origins of the Stokes Shift in PbS Quantum Dots: Impact of Polydispersity, Ligands, and Defects. *ACS Nano* **2018**, *12* (3), 2838−2845.

(15) Pradhan, S.; Di Stasio, F.; Bi, Y.; Gupta, S.; Christodoulou, S.; Stavrinadis, A.; Konstantatos, G. High-Efficiency Colloidal Quantum Dot Infrared Light-Emitting Diodes via Engineering at the Supra-Nanocrystalline Level. *Nat. Nanotechnol.* **2019**, *14* (1), 72−79.

(16) Kirkwood, N.; Monchen, J. O. V.; Crisp, R. W.; Grimaldi, G.; Bergstein, H. A. C.; du Fossé, I.; van der Stam, W.; Infante, I.; Houtepen, A. J. Finding and Fixing Traps in II−VI and III−V Colloidal Quantum Dots: The Importance of Z-Type Ligand Passivation. *J. Am. Chem. Soc.* **2018**, *140* (46), 15712−15723.

(17) Ushakova, E. V.; Litvin, A. P.; Parfenov, P. S.; Fedorov, A. V.; Artemyev, M.; Prudnikau, A. V.; Rukhlenko, I. D.; Baranov, A. V. Anomalous Size-Dependent Decay of Low-Energy Luminescence from PbS Quantum Dots in Colloidal Solution. *ACS Nano* **2012**, *6* (10), 8913−8921.

(18) Ellingson, R. J.; Beard, M. C.; Johnson, J. C.; Yu, P.; Micic, O. I.; Nozik, A. J.; Shabaev, A.; Efros, A. L. Highly Efficient Multiple Exciton Generation in Colloidal PbSe and PbS Quantum Dots. *Nano Lett.* **2005**, *5* (5), 865−871.

(19) Nootz, G.; Padilha, L. A.; Levina, L.; Sukhovatkin, V.; Webster, S.; Brzozowski, L.; Sargent, E. H.; Hagan, D. J.; Van Stryland, E. W. Size Dependence of Carrier Dynamics and Carrier Multiplication in PbS Quantum Dots. *Phys. Rev. B* **2011**, *83* (15), No. 155302.

(20) Klimov, V. I.; Mikhailovsky, A. A.; McBranch, D. W.; Leatherdale, C. A.; Bawendi, M. G. Quantization of Multiparticle Auger Rates in Semiconductor Quantum Dots. *Science* **2000**, *287* (5455), 1011−1013.

(21) Zhang, Y.; Vafaie, M.; Xu, J.; Pina, J. M.; Xia, P.; Najarian, A. M.; Atan, O.; Imran, M.; Xie, K.; Hoogland, S.; Sargent, E. H. Electron-Transport Layers Employing Strongly Bound Ligands Enhance Stability in Colloidal Quantum Dot Infrared Photodetectors. *Adv. Mater.* **2022**, *34* (47), No. 2206884.

(22) Parmar, D. H.; M. Pina, J.; Zhu, T.; Vafaie, M.; Atan, O.; Biondi, M.; Najjariyan, A. M.; Hoogland, S.; Sargent, E. H. Controlled Crystal Plane Orientations in the ZnO Transport Layer Enable High-Responsivity, Low-Dark-Current Infrared Photodetectors. *Adv. Mater.* **2022**, *34* (17), No. 2200321.

(23) Simone, G.; Dyson, M. J.; Weijtens, C. H. L.; Meskers, S. C. J.; Coehoorn, R.; Janssen, R. A. J.; Gelinck, G. H. On the Origin of Dark Current in Organic Photodiodes. *Advanced Optical Materials* **2020**, *8* (1), No. 1901568.

(24) Ahmadi, M.; Wu, T.; Hu, B. A Review on Organic−Inorganic Halide Perovskite Photodetectors: Device Engineering and Fundamental Physics. *Adv. Mater.* **2017**, *29* (41), No. 1605242.

(25) Jung, B. K.; Woo, H. K.; Shin, C.; Park, T.; Li, N.; Lee, K. J.; Kim, W.; Bae, J. H.; Ahn, J.-P.; Ng, T. N.; Oh, S. J. Suppressing the Dark Current in Quantum Dot Infrared Photodetectors by Controlling Carrier Statistics. *Advanced Optical Materials* **2022**, *10* (2), No. 2101611.

(26) Chen, D.; Liu, Y.; Xia, B.; Chen, L.; Yang, Y.; Yang, G.; Liu, J.; Lu, S.; Ge, C.; Liu, P.; Yang, J.; Liang, G.; Lan, X.; Zeng, X.; Li, L.; Zhang, J.; Xiao, Z.; Gao, L.; Tang, J. Passivating 100 Facets of PbS Colloidal Quantum Dots via Perovskite Bridges for Sensitive and Stable Infrared Photodiodes. *Adv. Funct. Mater.* **2023**, *33* (1), No. 2210158.

(27) Barkhouse, D. A. R.; Pattantyus-Abraham, A. G.; Levina, L.; Sargent, E. H. Thiols Passivate Recombination Centers in Colloidal Quantum Dots Leading to Enhanced Photovoltaic Device Efficiency. *ACS Nano* **2008**, *2* (11), 2356−2362.

(28) Tang, J.; Kemp, K. W.; Hoogland, S.; Jeong, K. S.; Liu, H.; Levina, L.; Furukawa, M.; Wang, X.; Debnath, R.; Cha, D.; Chou, K. W.; Fischer, A.; Amassian, A.; Asbury, J. B.; Sargent, E. H. Colloidal-Quantum-Dot Photovoltaics Using Atomic-Ligand Passivation. *Nat. Mater.* **2011**, *10* (10), 765−771.

(29) Arca, F.; Tedde, S. F.; Sramek, M.; Rauh, J.; Lugli, P.; Hayden, O. Interface Trap States in Organic Photodiodes. *Sci. Rep* **2013**, *3* (1), 1324.

(30) Pecunia, V.; Yuan, Y.; Zhao, J.; Xia, K.; Wang, Y.; Duhm, S.; Portilla, L.; Li, F. Perovskite-Inspired Lead-Free Ag2BiI5 for Self-Powered NIR-Blind Visible Light Photodetection. *Nano-Micro Lett.* **2020**, *12* (1), 27.

(31) Vafaie, M.; Fan, J. Z.; Morteza Najarian, A.; Ouellette, O.; Sagar, L. K.; Bertens, K.; Sun, B.; García de Arquer, F. P.; Sargent, E. H. Colloidal Quantum Dot Photodetectors with 10-Ns Response Time and 80% Quantum Efficiency at 1,550 Nm. *Matter* **2021**, *4* (3), 1042−1053.

(32) Thon, S. M.; Ip, A. H.; Voznyy, O.; Levina, L.; Kemp, K. W.; Carey, G. H.; Masala, S.; Sargent, E. H. Role of Bond Adaptability in the Passivation of Colloidal Quantum Dot Solids. *ACS Nano* **2013**, *7* (9), 7680−7688.

(33) Hines, M. a.; Scholes, G. d. Colloidal PbS Nanocrystals with Size-Tunable Near-Infrared Emission: Observation of Post-Synthesis Self-Narrowing of the Particle Size Distribution. *Adv. Mater.* **2003**, *15* (21), 1844−1849.